UC Santa Cruz
UC Santa Cruz Previously Published Works

Title

Ho2O3-TiO2 Nanobelts Electrode for Highly Selective and Sensitive Detection of Cancer miRNAs

Authors

Cui, Jingjie
Wang, Xuping
Chen, Shaowei

Peer reviewed

Article

Ho$_2$O$_3$-TiO$_2$ Nanobelts Electrode for Highly Selective and Sensitive Detection of Cancer miRNAs

Jingjie Cui [1,*] iD **, Xuping Wang** [1] **and Shaowei Chen** [2] iD

1   School of Automation, Hangzhou Dianzi University, Hangzhou 310018, China
2   Department of Chemistry and Biochemistry, University of California, 1156 High Street,
     Santa Cruz, CA 95064, USA
*   Correspondence: cuijingjie@hdu.edu.cn; Tel.: +86-57186878667

Abstract: The design and engineering of effective electrode materials is critical in the development of electrochemical sensors. In the present study, Ho$_2$O$_3$-TiO$_2$ nanobelts were synthesized by an alkaline hydrothermal process. The structure and morphology were investigated by X-ray diffraction (XRD) and field emission scanning electron microscope (FESEM) measurements. The Ho$_2$O$_3$-TiO$_2$ nanobelts showed a distinctly enhanced (004) reflection peak and rough surfaces and were used for the electrochemical selective sensing of various cancer miRNAs, such as prostate cancer miR-141, osteosarcoma miR-21, and pancreatic cancer miR-1290. Voltammetric measurements showed an oxidation peak at +0.4, +0.2, and +1.53 V for the three different cancer biomarkers, respectively, with the detection limit as low as 4.26 aM. The results suggest that the Ho$_2$O$_3$-TiO$_2$ nanobelts can be used as active materials to detect early cancers, for in vitro screening of anticancer drugs, and molecular biology research.

Keywords: Ho$_2$O$_3$-TiO$_2$; miRNA; detection; selective; sensitive; electrochemical

1. Introduction

Cancer is the most threatening disease in human life and health, and cancer research has been attracting extensive attention. As miRNAs are closely related to disease and it is generally believed that changes in nucleic acid molecules are the most critical primordial links of cell carcinogenesis, the research on miRNAs is important for the early diagnosis and immunotherapy of cancer [1]. For instance, recent studies have shown that miR-141 is a potentially useful biomarker for prostate cancer for the up-regulation in prostate cancer specimens [2]. MiR-21 plays an important role in developing osteosarcoma and can be used as a potential serum marker for it [3]. The content of miR-1290 will increase during the development of pancreatic cancer, so the determination of miR-1290 can be exploited for the early detection of pancreatic cancer [4]. However, current miRNA research and detection generally require complex pretreatment steps, expensive optical instruments, and fluorescent reagents [1]. Therefore, it is of great significance to develop rapid, sensitive, simple, and accurate miRNA detection methods that can be used for practical applications in life science research and medical and clinical diagnosis [5].

Nanomaterials have broad applications in the life sciences due to their unique physical and chemical properties and structural characteristics. Of these, titanium dioxide (TiO$_2$) nanostructures have been exploited for the sensitive, accurate, rapid, and simple detection and diagnosis of cancer, e.g., nano-p–n junction heterostructures, NiO/TiO$_2$ nanobelts for the detection of anticancer drugs and biointeractions with cancer cells [6], Au/TiO$_2$ bi-heterostructured nanobelts for the specific sensing of diverse tumour cells [7], mesoporous TiO$_2$ for the sensing of pancreatic cancer miR-1290 [8], rutile TiO$_2$ facet heterojunction nanostructure nuclease for the detection of miR-155 [9], and TiO$_2$ nanotube arrays for the detection of prostate protein antigen [10], among others.

For electrochemical biosensors, the active sensing material on the electrode acts as a catalyst that promotes the reaction of biochemical molecules to produce output signals [11]. The catalytic activity is the key factor in the selection and development of sensing materials which can be further manipulated by the doping of select rare earth elements [12] or the introduction of oxygen vacancies [13]. Holmium trioxide, Ho_2O_3, is an important rare earth metal (lanthanide) oxide with attractive electrical and optical properties. It has been widely used in environmental protection [14–16], functional ceramics [17,18], and sensing devices [19]. Mortazavi-Derazkola and coworkers [16] synthesized nano-Ho_2O_3 and observed an outstanding photocatalytic performance. Pan reported a high-k Ho_2O_3 sensing film for a pH ion-sensitive field-effect transistor (ISFET) [19]. Additionally, when Ho_2O_3 is doped into TiO_2, Ti^{4+} is partly replaced by Ho^{3+}, leading to the formation of abundant oxygen vacancies in TiO_2 and hence enhancing bulk conductivity and surface electrocatalytic activity. This will ultimately improve the electrochemical sensing activity of TiO_2. However, to the best of our knowledge, there have been no reports on using Ho_2O_3-TiO_2 as active materials to detect cancer miRNAs.

In this work, Ho_2O_3-TiO_2 nanobelts are prepared by using an alkaline hydrothermal process and exhibited high specificity and sensitivity for the electrochemical detection of cancer miRNAs. Specifically, Ho_2O_3-TiO_2 nanobelts can selectively detect miR-141, miR-21, and miR-1290 at distinctly different potentials and achieve a limit of detection as low as 4.26 aM, which suggests that Ho_2O_3-TiO_2 nanobelts may be used as a promising electrode material for early cancer diagnosis, drug screening, and molecular biology research.

2. Materials and Methods

2.1. Materials

Titania P-25 (TiO_2, ca. 75 wt.% anatase and 25 wt.% rutile, Degussa Co., Frankfurt, Germany), Ho_2O_3, and sodium hydroxide, were purchased from China National Reagents Corporation Ltd. (Shanghai, China). MicroRNA oligonucleotides (cDNA) were purchased from TSINGKE, and purified by polyacrylamide gel electrophoresis (PAGE). Various target miRNAs (e.g., miR-1290, miR-141, miR-21) and related match or mismatch probes were mixed and heated at 90 °C for 2 min. The volume ratio of target miRNA to probe was 1:1. Samples were diluted to a final concentration of 0.9 μM hybridization solutions. RNase-free distilled water was used throughout all of the experiments.

2.2. Preparation of Ho_2O_3-TiO_2 Nanobelts

Titanate nanobelts were synthesized via a hydrothermal process in a concentrated NaOH aqueous solution. Briefly, 0.1 g of the P-25 precursor and 9 mg of the Ho_2O_3 powders were mixed with 20 mL of a 10 M NaOH aqueous solution, and underwent a hydrothermal treatment at 180 °C in a 25 mL Teflon-lined autoclave for 72 h. The resulting powders were then immersed in a 0.1 M HCl aqueous solution for 24 h and washed thoroughly with de-ionized water. Finally, the collected samples were dried and calcined at 600 °C for 2 h to obtain Ho_2O_3-TiO_2 nanobelts.

2.3. Structure Characterization

A Bruker D8 Advance powder X-ray diffractometer was used to investigate Ho_2O_3-TiO_2 nanobelts (a Cu-Kα source, $\lambda = 0.15406$ nm) at room temperature within the range of $2\theta = 10$ to $70°$. Field-emission scanning electron microscopy (Hitachi S-4800) was used to characterize the morphology and size of the synthesized Ho_2O_3-TiO_2 nanobelts.

2.4. Electrochemistry Tests

The working electrode is assembled as follows: a glassy carbon electrode (GCE, 3 mm diameter) was polished with 0.05 μm Al_2O_3 suspensions and rinsed extensively with anhydrous ethanol and de-ionized water, and then electrochemically cleaned in 0.5 M H_2SO_4 by cycling potentials between -0.3 and $+1.8$ V at 100 mV·s^{-1}. A nafion adhesive

and an ethanol suspension of Ho_2O_3-TiO_2 nanobelts (0.5 mg mL^{-1}) were drop-cast onto the cleaned GCE surface. After drying, the resulting electrodes were used as sensing electrodes.

Electrochemical measurements were performed in a three-electrode configuration. The working electrode is the Ho_2O_3-TiO_2 nanobelts-modified electrodes prepared above, a counter electrode (Pt foil with a geometric area of 1.0 cm^2), and an Ag/AgCl/KCl saturated reference electrode. An SWV positive and negative sweep were performed using a CHI660C electrochemical work station, and voltammetric data were acquired. The schematic diagram for experimental procedure is found in the Supplementary Materials (see Figure S1).

## 3. Results and Discussion

3.1. Structural Characterization

The synthesized nanobelts were first characterized by XRD measurements. Figure 1 shows the XRD patterns of (a) TiO_2 and (b) Ho_2O_3-TiO_2 nanobelts. It can be seen that TiO_2-(B) (black dots) and anatase (asterisks) coexist in the TiO_2 nanobelts (curve a) [20]; and for the Ho_2O_3-TiO_2 nanobelts (curve b), the diffraction peaks appear at 2θ = 29, 33, 48 and 59 (denoted by #) that can be assigned to the Ho_2O_3 (222), (400), (440) and (622) facets (JCPDS 74-1984) [19]. Moreover, it can be seen that the diffraction peaks of Ho_2O_3-TiO_2 are overall stronger than those of TiO_2, indicating the enhanced crystallinity of the former. For example, as compared to curve a, curve b shows a strong and narrow TiO_2 (004) diffraction peak, suggesting more {001} facets with a high surface energy in the Ho_2O_3-TiO_2 sample [21,22].
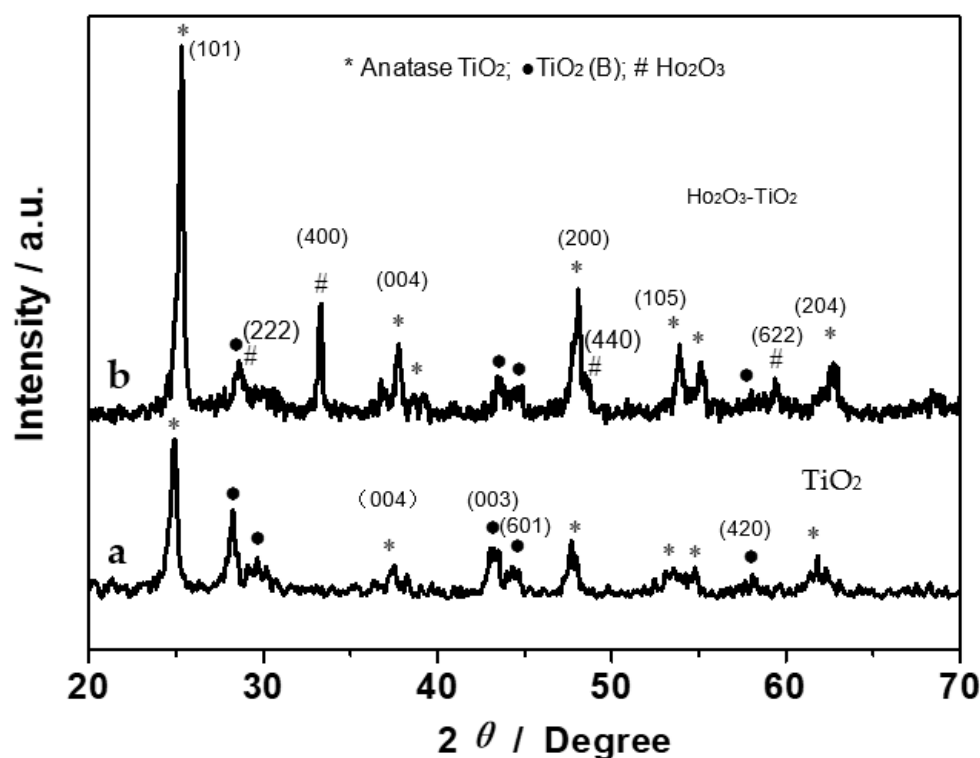
Figure 1. XRD patterns of (a) TiO_2 and (b) Ho_2O_3-TiO_2 nanobelts.

FESEM measurements were then carried out to investigate the nanobelts' morphology and microstructure. The morphology of the resulting sample exhibited a drastic change, as Ti^{4+} was partly replaced by Ho^{3+}. Compared to the TiO_2 nanobelts (Figure 2a,b), the Ho_2O_3-TiO_2 nanobelts were rougher, thinner, and shorter (Figure 2c,d). Usually, TiO_2 nanobelts grow along the c-axis of the anatase lattice, which makes them lack the {001} facets (Figure 2a,b). As depicted in Figure 1, the TiO_2 sample showed a relatively low and broad (004) peak. On the contrary, Ho_2O_3-TiO_2 nanobelts displayed a multiple-layer structure and were much thinner than TiO_2 nanobelts, and the surface was roughened, resulting in

a significant increase in the effective concentration of the {001} facets (Figure 2c,d). This is consistent with the enhanced (004) diffraction peak in Figure 1b. As Ti^{4+} was partly replaced by Ho^{3+}, oxygen vacancies might be produced in the Ho_2O_3-TiO_2 nanocrystals, and facilitated the transport of oxygen-containing species as an active material.
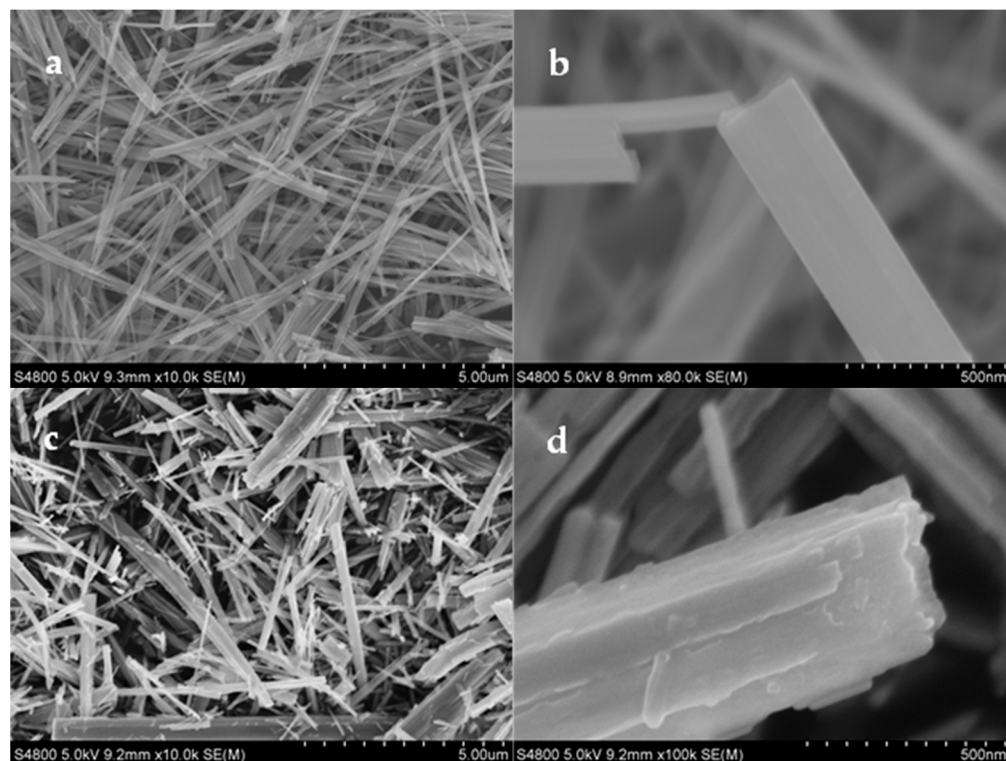
Figure 2. Representative SEM micrographs of (**a,b**) TiO_2 and (**c,d**) Ho_2O_3-TiO_2 nanobelts.

3.2. Specific and Sensitive Detection of Cancer miRNAs

As is well-known, miR-141, miR-21, and miR-1290 are specific biomarkers of prostate cancer, osteosarcoma, and pancreatic cancer, respectively. The Ho_2O_3-TiO_2 nanobelts prepared above were then used as a sensing electrode to detect these cancer microRNAs (Figures 3 and 4) by using square-wave voltammetry (SWV). Compared to other electrochemical techniques, SWV possesses the highest sensitivity and specificity in electrochemical pulse techniques.

Figure 3a shows the SWV positive sweep curves of the perfect match and mismatch for 5 fM prostate cancer miR-141 (related sequences see Table 1) hybridization solutions at the TiO_2 and Ho_2O_3-TiO_2 nanobelts modified electrodes. As compared with the featureless response at the TiO_2 nanobelts-modified electrode (Figure 3a(1)), there is a main anodic peak at +0.4 V and two minor ones at +0.9 V and +1.4 V, (Figure 3a(2)), corresponding to the electro-oxidation of perfect match miR-141 at the Ho_2O_3-TiO_2 nanobelts-modified electrodes, which indicates the enhanced electrochemical sensing of the miRNA by the Ho_2O_3-TiO_2 nanobelts. Additionally, for the Ho_2O_3-TiO_2 nanobelts-modified electrodes, no oxidation peak appears for all mismatch solutions within the potential range (Figure 3a(3–10)), which indicates that Ho_2O_3-TiO_2 nanobelts can selectively detect prostate cancer miRNA. The better sensing activity of Ho_2O_3-TiO_2 nanobelts can be explained by results from the XRD (Figure 1b) and FESEM (Figure 2c,d) measurements, where the {001} facets of Ho_2O_3-TiO_2 nanobelts were evidently increased due to the doping of Ho_2O_3. As is well known, anatase TiO_2 {001} facets are active for oxygen adsorption with a high activity [23]. As mentioned earlier, Ho_2O_3-TiO_2 nanobelts consisted of multiple layers and were much thinner than TiO_2 nanobelts, and had a roughened surface. This resulted in a significant increase of the effective concentration of the {001} facets and facilitated oxygen

adsorption on the Ho_2O_3-TiO_2 nanobelt surface, leading to the enhanced electroxidation of miR-141 at the Ho_2O_3-TiO_2 nanobelts electrodes [23]. Note that oxygen adsorption was not favored on stoichiometric anatase TiO_2 {001}, but can be enhanced by the introduction of oxygen vacancy [24]. Compared with the TiO_2 nanobelts, Ho_2O_3-TiO_2 nanobelts actually contained abundant oxygen vacancies due to the partial replacement of Ti^{4+} by Ho^{3+} [25], consistent with the enhanced sensing performance.
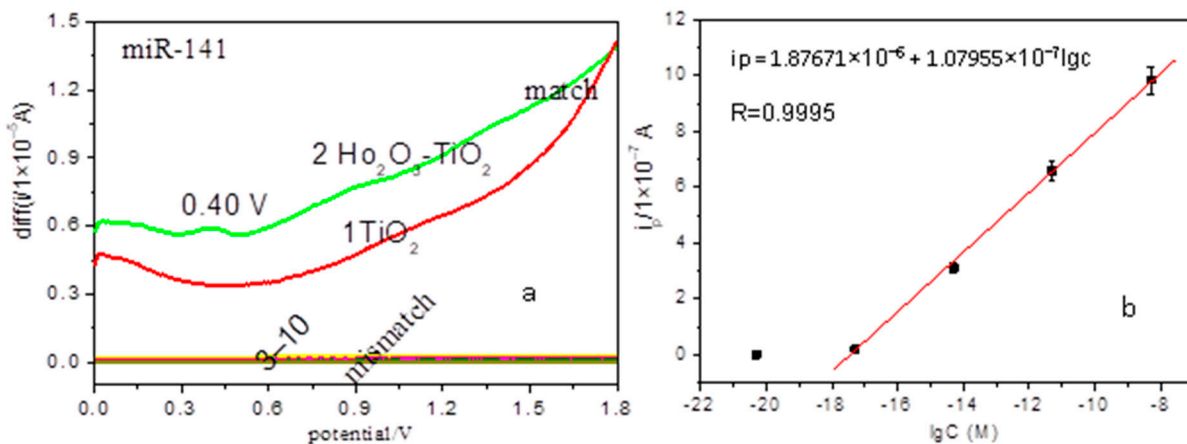
Figure 3. Electrochemical detection of cancer miRNAs. (**a**) SWV curves for miR-141: (1) match at the TiO_2 nanobelts modified electrode; match (2) and mismatch (3–10) at the Ho_2O_3-TiO_2 nanobelts modified electrodes; (**b**) Linear plot of anodic peak current (i_{pa}) versus concentration of perfect match miR-141 ranging from 0 to 5 nM at Ho_2O_3-TiO_2 nanobelts-modified electrodes.
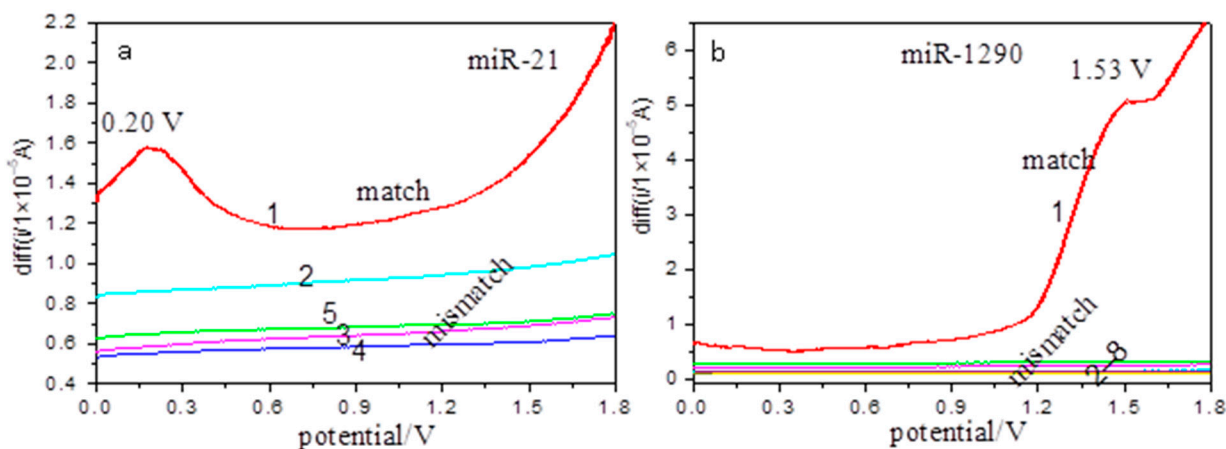
Figure 4. Electrochemical detection of cancer miRNAs at the Ho_2O_3-TiO_2 nanobelts-modified electrodes. SWV curves for (**a**) miR-21: match (1) and mismatch (2–5); (**b**) miR-1290: match (1) and mismatch (2–8).

Here, taking miR-141 as an example, we estimated the limit of detection of the Ho_2O_3-TiO_2 nanobelts modified electrode. Different concentrations of perfect match miR-141 were detected at the Ho_2O_3-TiO_2 nanobelts modified electrodes by using SWV measurements (see Figure S2). The variation of the anodic peak current (i_{pa}) versus concentration of perfect match miR-141 was shown in Figure 3b, which exhibited a linear correlation, $i_{pa}(A) = 1.87671 \times 10^{-6} + 1.07955 \times 10^{-7} \log(c)$ ($r^2 = 0.9995$) for the perfect match miR-141 within the concentration range of 0 to 5 nM. The i_{pa} of the blank sample was 1.2944×10^{-9} A at 0.4 V, so the final limit of detection was estimated to be 4.2658×10^{-18} M (or 4.26 aM). The sensitivity is higher than results previously reported for miRNA nano-biosensors [26].

Table 1. Matching and mismatching sequences for prostate cancer miR-141.

No.	miRNA	Squences
1,2	miR-141 Match probe Mismatch probes	5′-UAACACUGUCUGGUAAGAUGG-3′ 5′-CCATCTTTACCAGACAGTGTTA-3′
3		5′-ACATCTTTACCAGACAGTGTTA-3′
4		5′-GCATCTTTACCAGACAGTGTTA-3′
5		5′-TCATCTTTACCAGACAGTGTTA-3′
6		5′-CCATCTTTACCCGACAGTGTTA-3′
7		5′-CCATCTTTACCGGACAGTGTTA-3′
8		5′-CCATCTTTACCTGACAGTGTTA-3′
9		5′-CCATCTTTACCAGACAGTGTTC-3′
10		5′-CCATCTTTACCAGACAGTGTTG-3′

Note: mismatched nucleobases are underlined. The serial number in Table 1 is consistent with Figure 3a.

Under the same experimental conditions, detection of 0.9 μM osteosarcoma miR-21 and pancreatic cancer miR-1290 (related sequences in Tables 2 and 3) were also tested with the Ho_2O_3-TiO_2 nanobelts-modified electrodes (Figure 4). From Figure 4, it can be seen that the perfect match miR-21 and miR-1290 showed an oxidation peak at +0.2 V (Figure 4a) and +1.53 V (Figure 4b), respectively. Similarly, no oxidation peaks appear for all mismatch solutions within the same potential range (Figure 4a(2–5),b(2–8)). These results further confirmed that the Ho_2O_3-TiO_2 nanobelts-modified electrodes could selectively detect cancer miRNAs at distinctly different potentials.

Table 2. Matching and mismatching sequences for osteosarcoma miR-21.

No.	miRNA	Squences
1	miR-21 Match probe Mismatch probes	5′-TAGCTTATCAGACTGATGTTGA-3′ 5′-TCAACATCAGTCTGATAAGCTA-3′
2		5′-TCAACATCAGTGTGATAAGCTA-3′
3		5′-TCAACATCAGTTTGATAAGCTA-3′
4		5′-TCAACATCAGTCTGATCAGCTA-3′
5		5′-TCAACATCAGTCTGATAAGATA-3′

Note: mismatched nucleobases are underlined. The serial number in Table 2 is consistent with Figure 4a.

Table 3. Matching and mismatching sequences for pancreatic cancer miR-1290.

No.	miRNA	Squences
1	miR-1290 Match probe Mismatch probes	5′-TGGATTTTTGGATCAGGGA-3′ 5′-TCCCTGATCCAAAAATCCA-3′
2		5′-TCCCTGATCAAAAAATCCA-3′
3		5′-TCCCTGATCGAAAAATCCA-3′
4		5′-TCCCTGATCTAAAAATCCA-3′
5		5′-TCGCTGATCCAAAAATCCA-3′
6		5′-TCCCGGATCCAAAAATCCA-3′
7		5′-TCCCTGATCCAAACATCCA-3′
8		5′-TCCCTGATCCAAAAATACA-3′

Note: mismatched nucleobases are underlined. The serial number in Table 3 is consistent with Figure 4b.

The high selectivity of miRNA detections by Ho_2O_3-TiO_2 nanobelts can be explained within the context of the molecular structure. MiR-141, miR-21, and miR-1290 exhibit different base sequences and different molecular structures. They can form different hybrid bistrand structures with their respective match probe, which exhibits electrooxidation peaks at different potentials [7]. As shown in Figures 3 and 4, the different cancer miRNA (i.e., miR-141, miR-21, and miR-1290) showed specific voltammetric features, suggesting that

cancer miRNAs can be specifically detected via electrochemical potential sensing. Similarly, the perfect match and mismatch of these miRNAs have different hybrid bistrand structures. Compared with the perfect match, the mismatch nucleobases are exposed outside of the hybrid bistrand, resulting in different interactions between the miRNAs hybrid molecules and the electrode surface. Thus, the perfect match and mismatch of the cancer miRNAs exhibited a different electrochemical response, which was amplified by the formation of oxygen vacancy in Ho_2O_3-TiO_2 [24].

3.3. Mechanism of the Electrochemical Detection of Cancer

Within the present potential range, oxygen reduction reaction is inevitable (see Figure S3) [27]. Generally, the electrochemical reaction of O_2 in aqueous media can occur via a pathway involving intermediates such as H_2O_2 and O_2 (Equations (1)–(3)) [27,28]. The strong oxidants can enhance the electro-oxidation of miRNAs on the electrode surface. In comparison with TiO_2 nanobelts, the multiple layers and roughened surface of the Ho_2O_3-TiO_2 nanobelts effectively increased not only the specific surface area but also the concentration of the {001} facets (Figure 2), which further increased the active sites and promoted oxygen adsorption. Additionally, oxygen vacancies were formed in the Ho_2O_3-TiO_2 nanobelts since Ti^{4+} was partially replaced by Ho^{3+} (Equation (4)), and promoted oxygen adsorption on the anatase TiO_2 surface [24] as well as the diffusion of oxygen ions [29]. These collectively improved the surface electrocatalytic properties of the sensing electrodes [30]. Note that oxygen vacancies induced the surface adsorption of oxygen species in different states, i.e., the O-O bond in the superoxide state ($O_2^{-\bullet}$) was oriented parallel to the surface along the {010} facet, while the peroxide state (O_2^{2-}) was perpendicular to the surface along the {001} facet, which changed the microenvironment of the sensing electrode surface. Thus, it affects the sensitivity and specificity of the sensing electrodes. Additionally, as the oxygen vacancies are positively charged while miRNAs are negatively charged, the oxygen vacancies can promote the miRNAs adsorption and the oxygen species transfer (Scheme 1) [31,32], leading to enhanced electrochemical detection performance.

Scheme 1. The illustration for a mechanism of the electrochemical detection of cancer miRNAs.

Additionally, for the mismatched miRNA moleculars, the exposed mismatch bases increase the molecular steric hindrance, and nucleobases have hydrophobicity, all of which affect the mismatched miRNA moleculars' adsorption on the Ho_2O_3-TiO_2 electrode surface, resulting in their poor electrochemical sensing response.

$$O_2 + 2H^+ + 2e^- \rightarrow H_2O_2 \tag{1}$$

$$H_2O_2 + 2H^+ + 2e^- \rightarrow 2H_2O \tag{2}$$

$$H_2O_2 \rightarrow 2H_2O + O_2 \tag{3}$$

$$Ho_2O_3 \overset{2TiO_2}{\rightarrow} 2Ho'_{Ti} + V''_o + 3O_o \tag{4}$$

4. Conclusions

In this work, Ho_2O_3-TiO_2 nanobelts were successfully prepared and used as sensing active materials to detect cancer miRNAs. XRD and FESEM measurements indicated an efficient increase of the {001} facets in the nanobelts due to Ho_2O_3 doping. Electrochemical measurements showed that Ho_2O_3-TiO_2 nanobelts could selectively and sensitively detect cancer miRNAs. These results suggest that Ho_2O_3-TiO_2 nanobelts may serve as promising active materials for biosensing applications of early cancer diagnosis, drug screening, and molecular biology research.

References

1. Cheng, Y.; Dong, L.; Zhang, J.; Zhao, Y.Q.; Li, Z.P. Recent advances in microRNA detection. *Analyst* **2018**, *143*, 1758–1774. [CrossRef] [PubMed]
2. Jou, F.J.; Lu, C.H.; Ou, Y.C.; Wang, S.S.; Hsu, S.L.; Willner, I.; Ho, J.A. Diagnosing the miR-141 prostate cancer biomarker using nucleic acid-functionalized CdSe/ZnS QDs and telomerase. *Chem. Sci.* **2015**, *6*, 659–665. [CrossRef] [PubMed]
3. Wang, S.F.; Ma, F.; Feng, Y.; Liu, T.; He, S.S. Role of exosomal miR-21 in the tumor microenvironment and osteosarcoma tumorigenesis and progression (Review). *Int. J. Oncol.* **2020**, *56*, 1055–1063. [CrossRef] [PubMed]
4. Li, A.; Yu, J.; Kim, H.; Wolfgang, C.L.; Canto, M.I.; Hruban, R.H.; Goggins, M. MicroRNA array analysis finds elevated serum miR-1290 accurately distinguishes patients with low-stage pancreatic cancer from healthy and disease controls. *Clin. Cancer Res.* **2013**, *19*, 3600–3610. [CrossRef] [PubMed]
5. D'Agata, R.; Spoto, G. Advanced methods for microRNA biosensing: A problem-solving perspective. *Anal. Bioanal. Chem.* **2019**, *411*, 4425–4444. [CrossRef]
6. Cui, J.J.; Ge, Y.K.; Chen, S.W.; Liu, H.; Huang, Z.; Jiang, H.D.; Chen, J. Nano-p–n junction heterostructure TiO_2 nanobelts for the electrochemical detection of anticancer drug and biointeractions with cancer cells. *J. Mater. Chem. B* **2013**, *1*, 2072–2077. [CrossRef]
7. Cui, J.J.; Chen, J.; Chen, S.W.; Gao, L.; Xu, P.; Li, H. Au/TiO_2 nanobelt heterostructures for the detection of cancer cells and anticancer drug activity by potential sensing. *Nanotechnology* **2016**, *27*, 095603. [CrossRef]
8. Wang, X.P.; Cui, J.J.; Chen, S.W.; Yang, Y.; Gao, L.; He, Q.F. Electrochemical sensing of pancreatic cancer miR-1290 based on yeast-templated mesoporous TiO_2 modified electrodes. *Anal. Chim. Acta* **2020**, *1105*, 82–86. [CrossRef]
9. Liu, S.X.; Li, J.K.; Jiang, C.L.; Huang, L.; Qiao, B.; Lv, C.Z. Rutile Titanium Dioxide Facet Heterojunction Nanostructure with Double-Stranded Specific Nuclease for Photoelectrochemical MicroRNA-155 Detection. *Appl. Nano Mater.* **2022**, *5*, 2266–2272. [CrossRef]

10. Tian, C.Y.; Wang, L.; Luan, F.; Zhuang, X.M. An electrochemiluminescence sensor for the detection of prostate protein antigen based on the graphene quantum dots infilled TiO_2 nanotube arrays. *Talanta* **2019**, *191*, 103–108. [CrossRef]

11. Cui, J.J.; Sun, D.H.; Zhou, W.J.; Liu, H.; Hu, P.G.; Ren, N.; Qin, H.M.; Huang, Z.; Lin, J.J.; Ma, H.Y. Electrocatalytic oxidation of nucleobases by TiO_2 nanobelts. *Phys. Chem. Chem. Phys.* **2011**, *13*, 9232–9237. [CrossRef] [PubMed]

12. Akah, A. Application of rare earths in fluid catalytic cracking: A review. *J. Rare Earths* **2017**, *35*, 941–956. [CrossRef]

13. Wang, Z.L.; Mao, X.; Chen, P.; Xiao, M.; Monny, S.A.; Wang, S.C.; Konarova, M.X.N.; Du, A.J.; Wang, L.Z. Understanding the Roles of Oxygen Vacancy in Hematite based Photoelectrochemical Process. *Angew. Chem. Int. Ed.* **2019**, *58*, 1030–1034. [CrossRef] [PubMed]

14. Sahar, Z.A.; Sobhan, M.D.; Masoud, S.N. Simple sonochemical synthesis of Ho_2O_3-SiO_2 nanocomposites as an effective photocatalyst for degradation and removal of organic contaminant. *Ultrason. Sonochem.* **2017**, *39*, 452–460.

15. Zhao, X.N.; Liu, X.Z.; Lu, D.Z.; Wu, P.; Yan, Q.Y.; Liu, M.; Fang, P.F. Synergistic effect of Fe_2O_3/Ho_2O_3 Co-modified 2D-titanate heterojunctions on enhanced photocatalytic degradation. *Solid State Sci.* **2017**, *63*, 42–53. [CrossRef]

16. Sobhan, M.D.; Sahar, Z.A.; Masoud, S.N. Facile hydrothermal and novel preparation of nanostructured Ho_2O_3 for photodegradation of eriochrome black T dye as water pollutant. *Adv. Powder Technol.* **2017**, *28*, 747–754.

17. Hu, W.; Chen, Z.; Lu, Z.; Wang, X.; Fu, X. Effect of Bi_2O_3 and Ho_2O_3 co-doping on the dielectric properties and temperature reliability of X8R $BaTiO_3$-based ceramics. *Ceram. Int.* **2021**, *47*, 24982–24987. [CrossRef]

18. Heiba, Z.K.; Mohamed, M.B. Structural and magnetic properties of Mn doped Ho_2O_3 nanocrystalline. *J. Mol. Struct.* **2015**, *1105*, 135–140. [CrossRef]

19. Pan, T.M.; Huang, M.D. Structural properties and sensing characteristics of high-k Ho_2O_3 sensing film-based electrolyte–insulator–semiconductor. *Mater. Chem. Phys.* **2011**, *129*, 919–924. [CrossRef]

20. Chen, S.S.; Zhu, Y.H.; Li, W.; Liu, W.J.; Li, L.C.; Yang, Z.H.; Liu, C.; Yao, W.J.; Lu, X.H.; Feng, X. Synthesis, Features, and applications of mesoporous titania with TiO2(B). *Chin. J. Catal.* **2010**, *31*, 605–614. [CrossRef]

21. Yang, H.G.; Sun, C.H.; Qiao, S.Z.; Zou, J.; Liu, G.; Smith, S.C.; Cheng, H.M.; Lu, G.Q. Anatase TiO_2 single crystals with a large percentage of reactive facets. *Nature* **2008**, *453*, 638–642. [CrossRef] [PubMed]

22. Chen, X.B.; Mao, S.S. Titanium dioxide nanomaterials: synthesis, properties, modifications, and applications. *Chem. Rev.* **2007**, *107*, 2891–2959. [CrossRef] [PubMed]

23. Zeng, W.; Liu, T.; Wang, Z.; Tsukimoto, S.; Saito, M.; Ikuhara, Y. Oxygen Adsorption on Anatase TiO_2 (101) and (001) Surfaces from First Principles. *Mater. Trans.* **2010**, *51*, 171–175. [CrossRef]

24. Linh, N.H.; Nguyen, T.Q.; Diño, W.A.; Kasai, H. Effect of oxygen vacancy on the adsorption of O_2 on anatase TiO_2 (001): A DFT-based study. *Surf. Sci.* **2015**, *633*, 38–45. [CrossRef]

25. Tomić, M.; Šetka, M.; Chmela, O.; Gràcia, I.; Figueras, E.; Cané, C.; Vallejos, S. Cerium Oxide-Tungsten Oxide Core-Shell Nanowire-Based Microsensors Sensitive to Acetone. *Biosensors* **2018**, *8*, 116. [CrossRef]

26. Asadzadeh-Firouzabadi, A.; Zare, H. Preparation and application of AgNPs/SWCNTs nanohybrid as an electroactive label for sensitive detection of miRNA related to lung cancer. *Sens. Actuators B Chem.* **2018**, *260*, 824–831. [CrossRef]

27. Jörissen, L. Bifunctional oxygen/air electrodes. *J. Power Sources* **2006**, *155*, 23–32. [CrossRef]

28. Chi, X.W.; Tang, Y.G.; Zeng, X.Q. Electrode Reactions Coupled with Chemical Reactions of Oxygen, Water and Acetaldehyde in an Ionic Liquid: New Approaches for Sensing Volatile Organic Compounds. *Electrochim. Acta* **2016**, *216*, 171–180. [CrossRef]

29. Ji, Q.Q.; Bi, L.; Zhang, J.T.; Cao, H.J.; Zhao, X.S. The role of oxygen vacancies of ABO perovskite oxides in the oxygen reduction reaction. *Energy Environ. Sci.* **2020**, *13*, 1408–1428. [CrossRef]

30. Feng, H.F.; Xu, Z.F.; Ren, L.; Liu, C.; Zhuang, J.C.; Hu, Z.P.; Xu, X.; Chen, J.; Wang, J.; Hao, W.C.; et al. Activating Titania for Efficient Electrocatalysis by Vacancy Engineering. *ACS Catal.* **2018**, *8*, 4288–4293. [CrossRef]

31. Kousar, F.; Rasheed, U.; Khalil, R.M.A.; Niaz, N.A.; Hussain, F.; Imran, M.; Shakoor, U.; Algadi, H.; Ashiq, N. First principles investigation of oxygen vacancies filaments in polymorphic Titania and their role in memristor's applications. *Chaos Solitons Fractals* **2021**, *148*, 111024. [CrossRef]

32. Lu, J.; Qian, G.; Luo, L.; He, H.; Yin, S. Contributions of oxygen vacancies to the hydrogen evolution catalytic activity of tungsten oxides. *Int. J. Hydrogen Energy* **2021**, *46*, 676–682. [CrossRef]